

# The colour-magnitude relation of globular clusters in Centaurus and Hydra

## Constraints on star cluster self-enrichment with a link to massive Milky Way GCs

J. Fensch<sup>1,2</sup>, S. Mieske<sup>2</sup>, J. Müller-Seidlitz<sup>3</sup>, and M. Hilker<sup>3</sup>

<sup>1</sup> Ecole polytechnique, Route de Saclay, 91128, Palaiseau, France

<sup>2</sup> European Southern Observatory, Alonso de Cordova 3107, Vitacura, Santiago de Chile, Chile

<sup>3</sup> European Southern Observatory, Karl-Schwarzschild-Str. 2, 85748 Garching b. München, Germany

### ABSTRACT

**Aims.** We investigate the colour-magnitude relation of metal-poor globular clusters, the so called blue tilt, in the Hydra and Centaurus galaxy clusters and constrain the primordial conditions for star cluster self-enrichment.

**Methods.** We analyse U,I photometry for about 2500 globular clusters in the central regions of Hydra and Centaurus, based on FORS1@VLT data. We measure the relation between mean colour and luminosity for the blue and red subpopulation of the globular cluster samples. We convert these relations into mass-metallicity space and compare the obtained GC mass-metallicity relation with predictions from the star cluster self-enrichment model by Bailin & Harris (2009). For this we include effects of dynamical and stellar evolution and a physically well motivated primordial mass-radius scaling.

**Results.** We obtain a mass-metallicity scaling of  $Z \propto M^{0.27 \pm 0.05}$  for Centaurus GCs and  $Z \propto M^{0.40 \pm 0.06}$  for Hydra GCs, consistent with the range of observed relations in other environments. We find that the GC mass-metallicity relation already sets in at present-day masses of a few  $10^5 M_\odot$  and is well established in the luminosity range of massive MW clusters like omega Centauri. The inclusion of a primordial mass-radius scaling of star clusters significantly improves the fit of the self-enrichment model to the data. The self-enrichment model accurately reproduces the observed relations for average primordial half-light radii  $r_h \sim 1 - 1.5$  pc, star formation efficiencies  $f_\star \sim 0.3 - 0.4$ , and pre-enrichment levels of  $[Fe/H] - 1.7$  dex. The slightly steeper blue tilt for Hydra can be explained either by a  $\sim 30\%$  smaller average  $r_h$  at fixed  $f_\star \sim 0.3$ , or analogously by a  $\sim 20\%$  smaller  $f_\star$  at fixed  $r_h \sim 1.5$  pc. Within the self-enrichment scenario, the observed blue tilt implies a correlation between GC mass and width of the stellar metallicity distribution. We find that this implied correlation matches the trend of width with GC mass measured in Galactic GCs, including extreme cases like Omega Cen and M54.

**Conclusions.** First, we found that a primordial star cluster mass-radius relation provides a significant improvement to the self-enrichment model fits. Second we show that broadened metallicity distributions as found in some massive MW globular clusters may have arisen naturally from self-enrichment processes, without the need of a dwarf galaxy progenitor.

**Key words.** Stars: supernovae: general; Galaxy: globular clusters: general; Galaxies: star clusters: general; Stars: formation

## 1. Introduction

### 1.1. Colour magnitude relation of extragalactic globular clusters

The broadband colour distribution of globular clusters (GCs) exhibits a strong bimodality especially in globular cluster systems of massive galaxies (e.g. Gebhardt & Kissler-Patig 1999; Kundu & Whitmore 2001; Larsen et al. 2001), which is often interpreted as a result of star formation and galaxy assembly processes in the early universe (see the review of Brodie & Strader 2006). In the last decade, Hubble Space Telescope (HST) and ground-based wide-field imaging of hundreds of GC systems has provided us with very detailed information on bimodality (e.g. Dirsch et al. 2003, Bassino et al. 2006, Peng et al. 2006, Harris et al. 2006 & 2013, Forbes et al. 2011, Kartha et al. 2014).

One of the surprising outcomes of those studies is a correlation between colour and magnitude for GCs of the blue subpopulation (e.g. Harris et al. 2006, Strader et al. 2006, Mieske et al. 2006 & 2010, Spitler et al. 2006, Humphrey 2009,

Cockcroft et al. 2009, Harris et al. 2009a & 2009b, Forbes et al. 2010, Blom et al. 2012, Usher et al. 2013). This phenomenon has been nicknamed the blue tilt, and has also been detected through ground-based imaging (Forte et al. 2007, Wehner et al. 2008, Park 2012). The first strong hint of the existence of such a colour-magnitude relation of GCs was reported in Dirsch et al. (2003), who found that the colour distribution of the brightest GCs in NGC 1399 becomes broad and unimodal. Direct evidence from spectroscopic observations was recently reported for M31 GCs (Schiavone et al. 2013).

Interpreted as a mass-metallicity relation, the blue tilt is equivalent to a scaling with mass of  $Z \propto M^{0.3-0.7}$ , that depends on environment. Results have so far indicated that the trend sets in already at masses slightly below a million solar masses, at several  $10^5 M_\odot$ . The most common interpretation of this colour-metallicity relation is self-enrichment. With increasing primordial cluster mass (and thus increasing potential well depth), a larger fraction of SN II metal ejecta are kept in the cluster and reprocessed into a second generation of stars (Strader & Smith 2008, Bailin & Harris 2009). Furthermore a red tilt, i.e.

a colour magnitude relation for the red GC subpopulation, has been reported in some cases, but it typically is less significant and weaker in metallicity space (e.g. Harris et al. 2006, Mieske et al. 2006 & 2010).

It is worth noting that colour changes as a function of GC mass can also occur as a result of dynamical evolution, via preferential loss of low-mass stars (Kruijssen & Lamers 2008; Anders et al. 2009; Kruijssen 2009). This makes lower-mass GCs bluer than their colour for an unaltered stellar mass function, thus qualitatively creating a trend in the direction of the blue tilt. This effect was investigated for example in Mieske et al. (2010) and particularly in Goudfrooij et al. (2014) who studied how it depends on the shape of the Initial Mass Function (IMF). However, it is clear that the observed blue tilt can only be explained in small parts by this effect: the observations indicate a strengthening of the effect at high cluster masses (Harris et al. 2006, Mieske et al. 2010), exactly opposite to expectations from dynamical evolution: higher mass cluster are less affected by dynamical evolution (Baumgardt & Makino 2003), and thus colour changes from this effect will level off at higher cluster masses.

An important aspect to keep in mind is that the cluster-to-cluster scatter of mean metallicity due to local variations in primordial star forming conditions is significant, and will dominate smooth internal trends with cluster mass for small samples of globular clusters (see e.g. Bailin & Harris 2009). To filter out underlying trends like self-enrichment from broadband integrated photometry, one needs large homogeneous data sets of GCs, typically more than  $\sim 1000$  GCs. For example, for the Milky Way no blue tilt is detectable despite the considerable cluster-to-cluster scatter in mean  $[\text{Fe}/\text{H}]$  and the comparably small sample size (e.g. Strader & Smith 2008). Moreover, the Milky Way GC sample has a rather low upper-mass limit ( $M_{\omega\text{Cen}} = 1.5 * 10^6 M_{\odot}$ ), which is another factor for the non-detectability of the blue tilt in our Galaxy.

## 1.2. Multiple stellar populations in massive Galactic GCs

Almost parallel in time to the discovery of the blue tilt in extragalactic GC samples, HST imaging of individual stars in Galactic GCs also revealed striking new features: there are multiple stellar populations in almost every intermediate-to-high mass GC that has been studied in detail (e.g. Bedin et al. 2004, Piotto et al. 2005 & 2012, Milone et al. 2012a, 2012b, 2012c). This has further enhanced the interest in self-enrichment scenarios for star clusters. It is typically assumed that self-enrichment from SN ejecta are required to obtain a broadened stellar metallicity distribution of red giants as seen for example in  $\omega\text{Cen}$  and M54 (e.g. Willman & Strader 2012), for which a present-day onset mass of around a million solar masses is consistent with the data in the Milky Way. Re-processing of ejecta from evolved stars is, in turn, often considered a scenario for creating multiple populations at constant metallicity (e.g. Ventura et al. 2001, d’Antona et al. 2002 & 2005, D’Ercole et al. 2008, Maxwell et al. 2014), which can occur at about one order of magnitude lower cluster masses than enrichment from SN ejecta (Baumgardt et al. 2008).

## 1.3. This paper

In this paper we put special emphasis on how a fit of SN self-enrichment models to our data constrains the primordial structure and star formation conditions in massive star clusters.

We analyse the colour-magnitude relation of GCs in the central 100 kpc of the Hydra and Centaurus galaxy clusters. We use deep U-I imaging with FORS1@VLT at very good seeing. We analyse a sample of about 2500 GCs in each cluster, down to a limiting magnitude about 0.5 mag brighter than the GCLF turnover. The usage of the U-band gives us a very broad wavelength baseline that improves our metallicity resolution compared to other studies. Furthermore, our homogeneous data set allows us to perform a robust comparison between the two investigated environments.

The structure of the paper is as follows. In Sect. 2 we discuss the data reduction and selection of GC candidates. In Sect. 3 we measure the mass-metallicity relations of GCs in Hydra and Centaurus. In Sect. 4 we constrain a star cluster self-enrichment model by comparing its prediction to the measured relation. We focus on the inclusion of previously not considered physical features into the model, and on the degeneracy between the input parameters of the model. We also convert the global mass-metallicity relation into a mass-metallicity *spread* relation, and compare this to Milky Way GCs. We provide Summary and Conclusions in Sect. 5.

## 2. Data

### 2.1. Observations

The data analysed for this paper were all taken in service mode with FORS1@VLT. The I-band photometry was obtained in the course of programmes 065.N-0459 (Hydra, PI Hilker) and 067.A-0358 (Centaurus, PI Hilker), with 3000s integration time in I-band per  $7 \times 7'$  FORS pointing, at good seeing 0.4-0.7'' in seven FORS pointings in Centaurus and Hydra and one background pointing. Those data were already presented in Mieske et al. (2003, 2005) in an SBF analysis of both clusters. This I-band data set also comes along with V-band data taken in the same runs and under similar conditions. The V-band data is not used directly for our blue tilt analysis, but we use the V-I colour distribution to finetune the U-I colour calibration, see Sect. 2.2.1. For the present work, these I- (and V-) data were carefully re-reduced.

The U-band data was obtained in programmes 080.A-0647 & 082.A-0894 (PI Hilker) with about 0.8'' seeing, in three FORS pointings in Centaurus, two in Hydra and one background pointing in each cluster. The on-source integration in U-band was about 2 hours per pointing.

In Fig. 1 we show a colour-composite image of the two target clusters, created from the FORS imaging data in U,V,I. Fig. 2 shows a map with the projected positions of GC candidates with U,I photometry. The background fields are situated at  $\alpha = 189.78$ ,  $\delta = -41.35$  for Centaurus and  $\alpha = 160.9$ ,  $\delta = -27.48$  for Hydra, about  $2^\circ$  away from the respective cluster centres. More details on the reduction and analysis of the data will be given in a forthcoming paper (Hilker et al. 2014 in preparation).

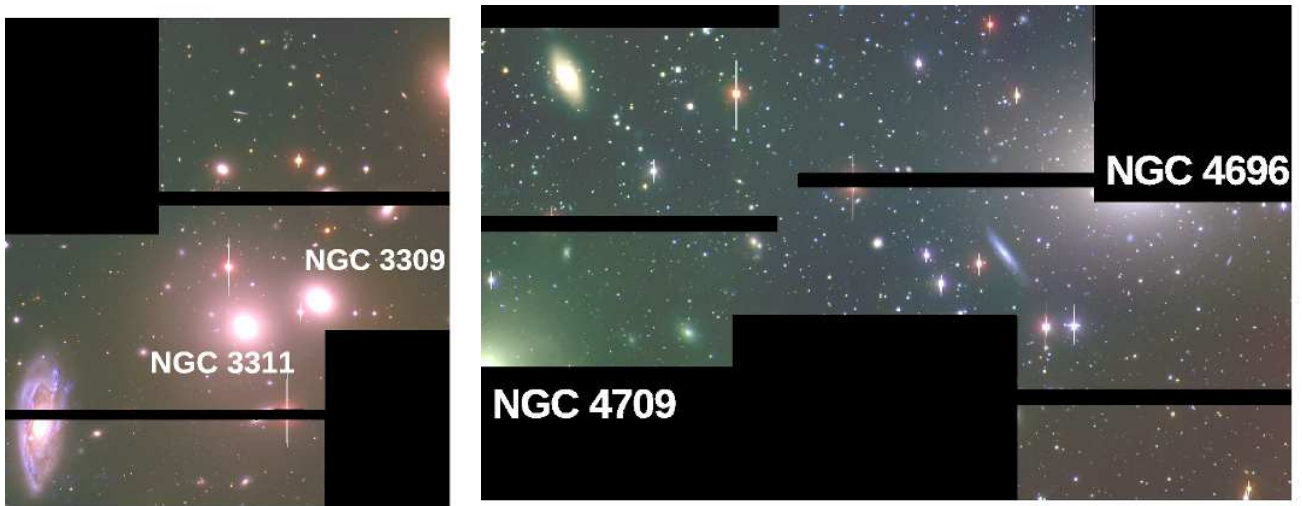


**Fig. 1.** FORS U,V,I composite-images showing the investigated region of the Hydra (left) and Centaurus (right) clusters. The two main central cluster galaxies are indicated. For Centaurus, the imaging covers the intra-cluster part between NGC 4696 and NGC 4709, while for Hydra the imaging is centred on NGC 3311. Projected physical scale is about 100x100 kpc per FORS pointing in Hydra, and 90x90 kpc in Centaurus (assuming a NED distance of 47.8 Mpc to Hydra and 43.2 Mpc to Centaurus).

## 2.2. Data Reduction

The raw data were processed with IRAF<sup>1</sup>. We performed standard bias subtraction, flat fielding and bad pixel removal. We then registered and combined the single integrations. The next step was to model and subtract the extended light from bright galaxies, to enable clean photometry of point source close to the galaxy centers. We did so using a combination of IRAF's *rme-dian* task, and galaxy light modelling with IRAF's *ellipse* task. Diffuse galaxy light is thus removed apart from their very central regions. The PSF photometry of point sources was performed with the standard IRAF routine *psf* within the *daophot* package.

Photometric calibration was done using regular standard star observations within ESO's calibration plan. We corrected relative offsets between different pointings (not all nights were photometric) by using overlap regions of adjacent fields, and using the central pointing in each cluster as reference. These relative calibrations worked very well for the I-band with residual inaccuracies of the level of 0.02-0.03 mag. However, the U-band data could not be calibrated down to this accuracy, given the low number of standard stars available in U, lower flux levels, and smaller overlap between adjacent fields. Therefore we applied an additional, relative U-I colour scale calibration between Hydra and Centaurus as described in the following.

### 2.2.1. Relative calibration of U-I colour scale

The top panels of Fig. 3 show the U-I (left) and V-I (right) colour distribution of sources detected in the background fields for Hydra and Centaurus. While the V-I distribution of both samples peaks at the same colour within the error bars, there is a shift of about 0.2 mag in U-I between Hydra and Centaurus. Using KMM (Ashman et al. 1994), the precise value of the shift is determined to be 0.22 mag. We interpret this colour shift as a residual systematic uncertainty of the U-band photometric calibration

in Hydra and Centaurus, as noted in the previous subsection. In order to compare the two samples on the same absolute colour scale, we add to the U-band an offset of -0.11 mag to Centaurus sources and +0.11 mag to Hydra in the following. The bottom panels of Fig. 3, which show the Centaurus and Hydra GC colour distribution in U-I, include those offsets.

## 2.3. Selection of Globular Clusters

The first step was to remove resolved sources by a combined cut-off in the IRAF PSF parameters  $\chi$  and *Sharpness*. This reduced the contamination by a factor of two.

The second step was to introduce a realistic colour cut-off condition that corresponds to the extreme U-I colours expected for GCs. Such values were taken from the metallicity distribution of Milky Way GCs obtained by Harris (1996, 2010 edition), that is  $[\frac{E}{H}] = -2.4$  and  $[\frac{E}{H}] = 0.3$ , converted into a U-I colour range of 1.3 to 3.0 mag using TERAMO models (Raimondo et al. 2005) evaluated at 11-13 Gyr age (Figs. 4 and 6). We broadened these borders by the maximum measurement error as a function of luminosity, as indicated by the solid lines in Fig. 4.

To remove the remaining contamination by unresolved foreground stars and background galaxies in the colour range expected for GCs, a comparison between the science field and the background field was done. For this we divided the colour-magnitude plane in cells with rows of 200 GCs and 0.1 mag colour width, see Fig. 4. Sources in Hydra and Centaurus were then randomly deleted in each cell according to the number of background points in the cell, and the respective ratio between the area coverage of cluster and background sample: 3:1 in Centaurus and 2:1 for Hydra.

After background subtraction, the final GC candidate sample comprised 2590 sources for Centaurus, and 2365 sources for Hydra.

<sup>1</sup> IRAF is distributed by the National Optical Astronomy Observatories, which are operated by the Association of Universities for Research in Astronomy, Inc., under cooperative agreement with the National Science Foundation.

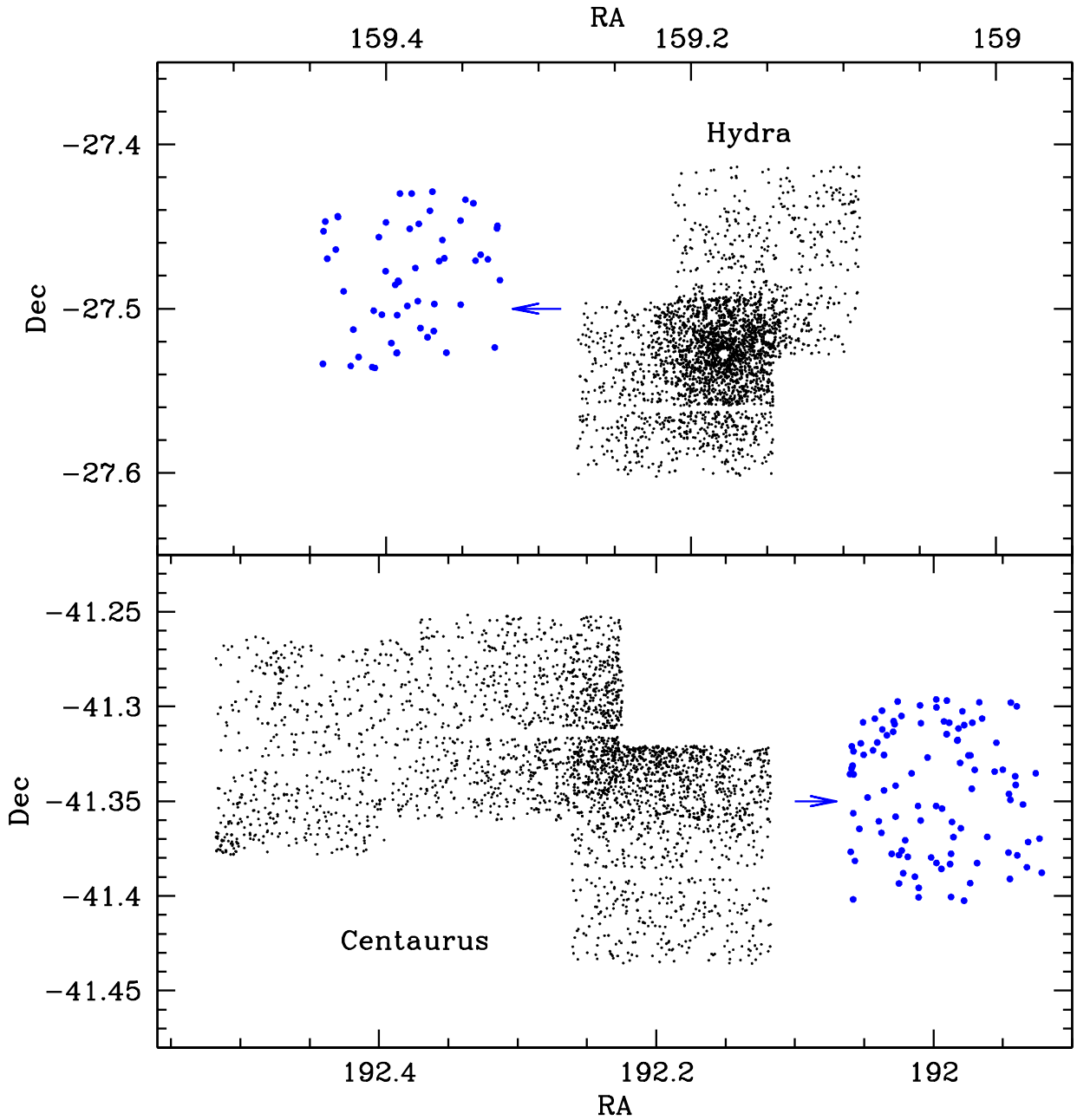


**Fig. 2.** Projected position of photometrically selected GC candidates in Hydra and Centaurus in our U-I FORS1 imaging data. See text for details on the GC selection. The sources detected in the background field with the same photometric selection criteria are indicated as (blue) dots for comparison. The actual location of the background field in each cluster was about 2 degrees away, in the direction indicated by the arrow. **Top:** Hydra. **Bottom:** Centaurus. Projected physical scale is about 100x100 kpc per FORS pointing in Hydra, and 90x90 kpc in Centaurus.

### 3. Data Analysis

#### 3.1. Fitting Procedure

To measure the colour of the blue and red peak as a function of GC luminosity, we applied a hybrid approach using both KMM and colour distribution medians (see also Mieske et al. 2006). This is outlined in the following.

In the bottom panel of Fig. 3 we show the U-I colour histogram of the GC candidates in Hydra and Centaurus, limited to  $I < 24$  mag. The distribution is not obviously bimodal, but does have a large tail towards red colours that cannot be fitted

by a single Gaussian. In that figure we indicate the fitted colour peaks using KMM, both in heteroscedastic and homoscedastic mode. It is clear that the output of both modes differ, indicating that the width of the blue and red peak are not identical. Therefore, a heteroscedastic fit is more appropriate to our sample than a homoscedastic fit.

At the same time, we found that such heteroscedastic fits increase the scatter between adjacent luminosity bins, i.e. when subdividing the sample into a number of smaller subsamples. Our aim in the fitting is to represent the heteroscedastic nature of our sample, but at the same time provide a stable peak deter-

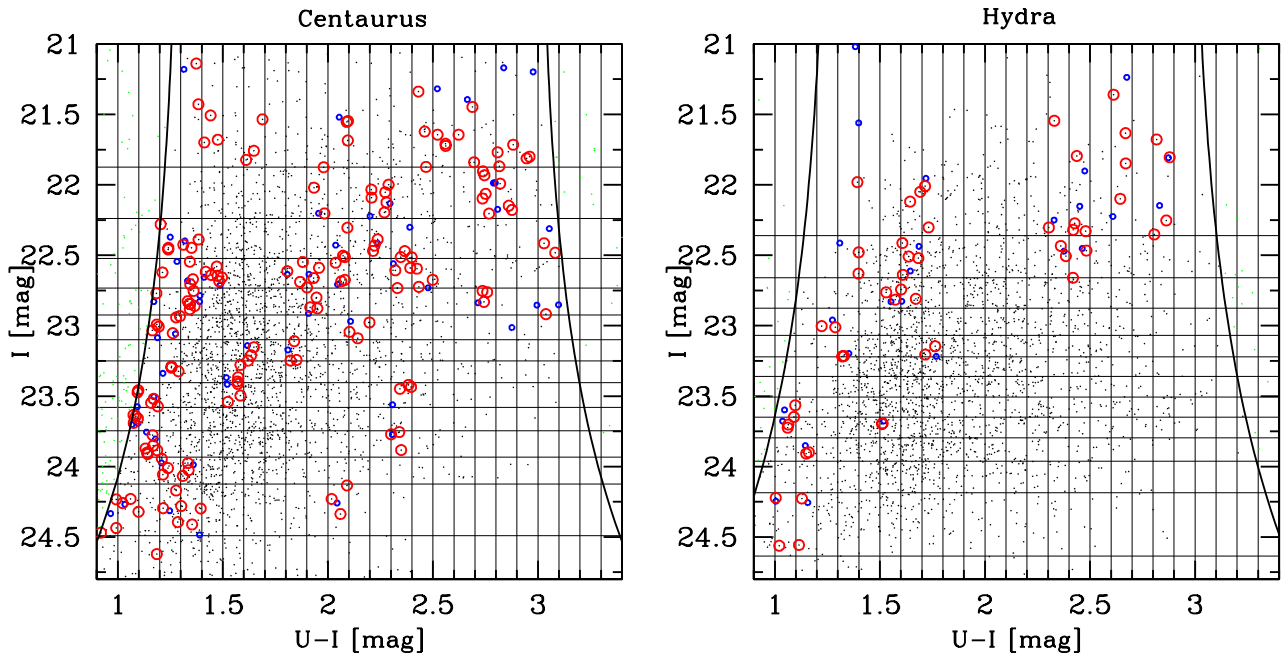


**Fig. 4.** Colour-Magnitude diagram in UI of all unresolved sources detected in both galaxy clusters. The black curved lines represent the colour cut-off applied to disregard sources either too blue or too red to be considered old GCs. The horizontal lines define rows of 200 GCs, and the vertical lines define columns of 0.1 mag. Within the cells defined by the horizontal and vertical lines, a random background subtraction is performed: The blue circles indicate colours and magnitudes of the background sources. Red circles indicate sources that were removed based on the background source distribution, within the indicated cells. We note that the very brightest magnitude regions  $I < 21\text{mag}$  are excluded from the plot to focus on the main body of GCs.

mination as a function of luminosity. Therefore we measured in each luminosity bin of 200 GCs the median colour blue- and redwards of a constant dividing line between blue and red sequences (see also Fig. 5 of Mieske et al. 2006), itself determined from a heteroscedastic KMM fit to the full sample. We adopt such a constant dividing line - as opposed to a limit that varies as a function of luminosity - to ensure that a distribution without any colour-magnitude relation would be correctly recovered. This limiting colour is  $U-I = 1.93\text{ mag}$  for Centaurus and  $1.99\text{ mag}$  for Hydra (Fig. 3). It corresponds to about  $[Fe/H] = -0.9\text{ dex}$ , within  $\sim 0.1\text{ dex}$  of the limit found in the Milky Way GC system (Harris et al. 1996, see e.g. Fig. 2 of Strader & Smith (2008)). Luminosities fainter than  $I=24\text{ mag}$  are not included for the fit because of a lack of faint red clusters (incompleteness) that would introduce a bias in our analysis.

In Fig. 5 we show the resulting blue and red peak colours as a function of GC luminosity for the Hydra and Centaurus samples. We note that this distribution is not 100% deterministic because of the background source subtraction that is performed randomly within colour-magnitude cells as described in Fig. 4. To take this into account for the fitting of the slope between colour and magnitude, we perform this fitting based on 100 different random background subtractions. To each individual run, we apply an unweighted least squares fit (each magnitude bin comprises the same number of data points) of a linear relation to these data points, whose slope we denote as  $\gamma = d(U - I)/d(I)$ .

We indicate the resulting average slopes and their error bars in Table 1, and also indicate the (small) additional statistical error arising from the random background subtraction. We obtain slopes for the blue peak of  $\gamma = -0.057 \pm 0.011$  for Centaurus and  $\gamma = -0.081 \pm 0.012$  for Hydra, thus finding a highly significant blue tilt in both clusters. A red tilt is also detected for Centaurus,

with  $\gamma = -0.086 \pm 0.015$ . The error bars are derived from the scatter of the data points with respect to the fitted relation.

### 3.2. Mass-Metallicity Relations

In the previous subsection we find a clear blue tilt for the Hydra and Centaurus cluster. To investigate this in more detail it is necessary to convert the colour-magnitude relation into a more physical mass-metallicity relation.

To this end, we convert I-band magnitude into mass using:

- A colour-independent mass-to-light ratio of  $\Gamma = 2.2$ , based on the models of Maraston (2005) and Bruzual & Charlot (2003).
- A NED distance of 47.8 Mpc to Hydra and 43.2 Mpc to Centaurus.
- An absolute magnitude  $M_I = 4.13\text{ mag}$  of the Sun. The resulting mass range of GCs is  $\sim 5 \times 10^5$  to  $5 \times 10^6$  solar masses.

Colour  $U-I$  is converted into metallicity using a piecewise linear function representing the TERAMO Models (Raimondo et al. Raimondo et al. (2005)) for an assumed age of 11-13 Gyr, see Fig. 6. We adopt two lines of different slopes that intersect at  $U-I=2.07$ , which is accurate to within 0.1 dex compared to the model predictions. The conversion from  $U-I$  to  $[Fe/H]$  thus is

$$[Fe/H] = -0.702 + 1.94 \times [(U - I) - 2.0688] \quad (1)$$

for  $(U - I) \leq 2.0688$  ( $[Fe/H] \leq -0.702$ ). And,

$$[Fe/H] = -0.702 + 1.04 \times [(U - I) - 2.0688] \quad (2)$$

for  $(U - I) > 2.0688$  ( $[Fe/H] > -0.702$ ).



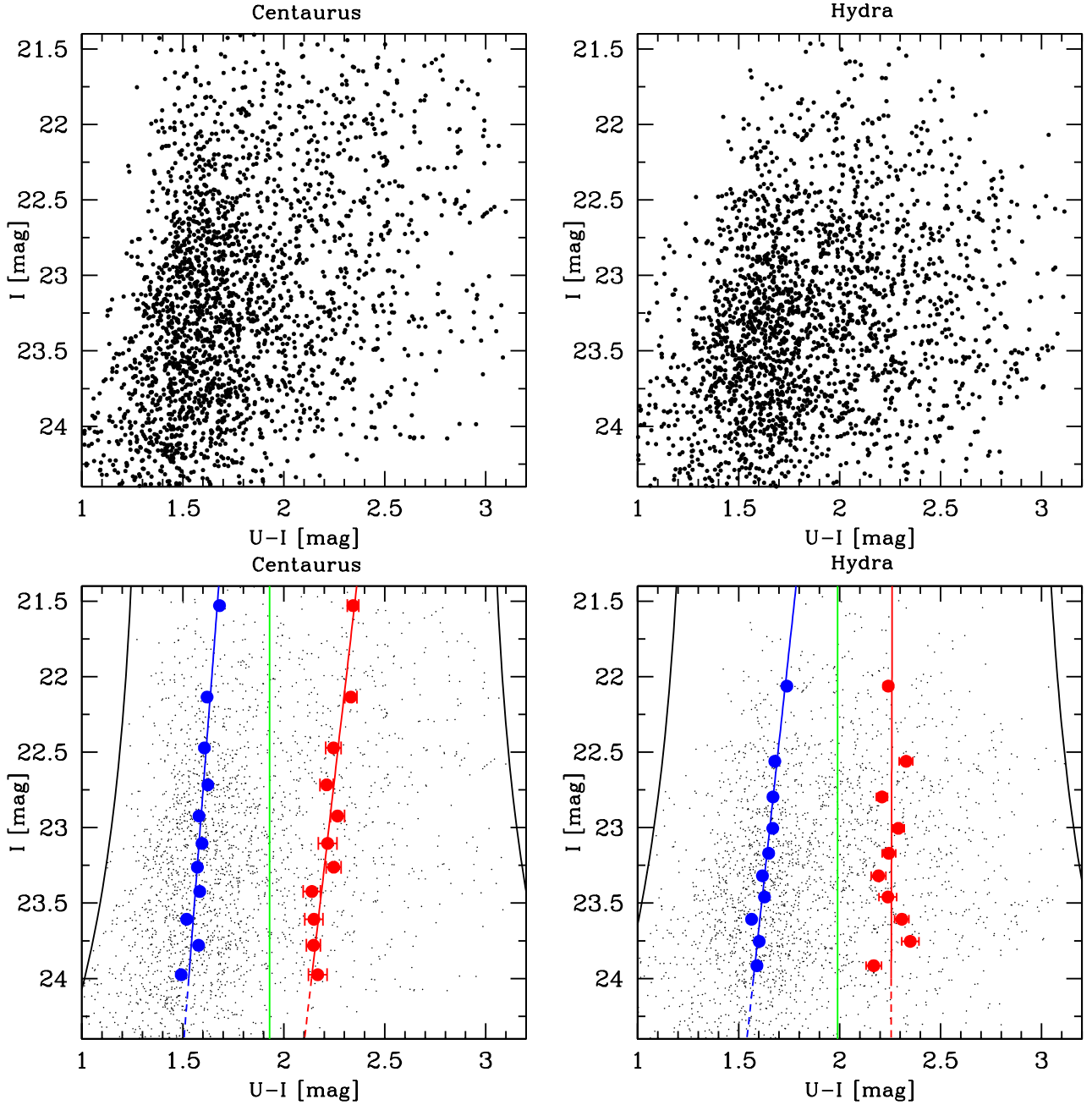


**Fig. 5.** Colour-Magnitude Diagrams of the final GC samples for Centaurus (left) and Hydra (right). The individual data points in the top and bottom plot are the same. In the bottom plots additional filled circles in blue and red indicate the median colours between the black limiting curves at extreme colours and the (green) fixed dividing line between the blue and red peak. The blue and red lines indicate least squares fits to the median colours as a function of magnitude.

**Table 1.** Value of the blue tilt slope  $\gamma = d(U - I)/dI$  and of the Mass-Metallicity relation exponent  $\alpha$  obtained for Centaurus and Hydra with our data for the range  $I < 24.0$  mag, compared to results of previous studies on these clusters and other environments. In brackets we also indicate the errors arising from the randomised background subtraction in magnitude-colour cells.

Sample	$\gamma$ blue	$\alpha$ blue ( $Z \propto M^\alpha$ )	$\gamma$ red	$\alpha$ red ( $Z \propto M^\alpha$ )
Centaurus	$-0.057 \pm 0.011$ [ $\pm 0.003$ ]	$0.27 \pm 0.05$	$-0.086 \pm 0.015$ [ $\pm 0.002$ ]	$0.22 \pm 0.04$
Hydra	$-0.081 \pm 0.012$ [ $\pm 0.005$ ]	$0.40 \pm 0.06$	$-0.002 \pm 0.034$ [ $\pm 0.004$ ]	$0.01 \pm 0.09$
Hydra (Wehner et al. 2008)		$0.60 \pm 0.20$		
BCGs (Harris et al. 2009a)		$0.48 \pm 0.12$		$-0.11 \pm 0.06$
M104 (Harris et al. 2010)		$0.29 \pm 0.04$		
FCS (Mieske et al. 2010)		$0.38 \pm 0.08$		$0.03 \pm 0.05$
VCS (Mieske et al. 2010)		$0.62 \pm 0.08$		$0.12 \pm 0.05$

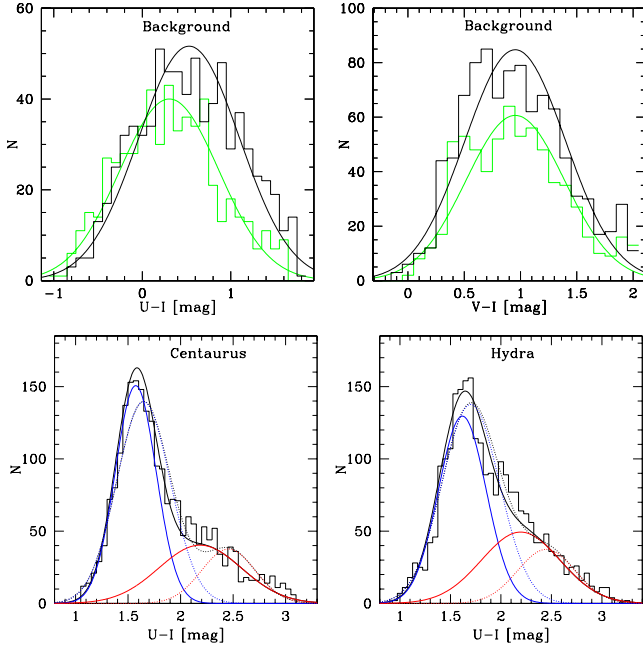


**Fig. 3.** **Top:** Colour distribution of the background fields: Centaurus is in black and Hydra in green. **Left panel:** U-I. **Right panel:** V-I. The lines correspond to single Gaussian peaks fitted with KMM. Because of the shift in U-I between both clusters, symmetric shifts of  $\pm 0.11$  mag are applied to the U-band zeropoints for Hydra and Centaurus, see text for details. **Bottom:** Finally adopted U-I colour distribution of the full Hydra (left) and Centaurus (right) cluster GC samples (restricted to the later used fitting range  $I < 24$  mag). The coloured lines represent the Gaussian fits by KMM to the blue and red peak. The black lines are the sum of the two. The dotted lines represent the results using the homoscedastic mode; the solid lines correspond to the heteroscedastic mode.

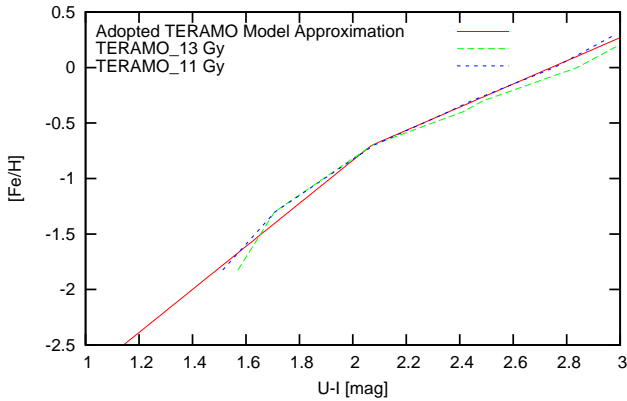


**Fig. 6.** Metallicity [Fe/H] as a function of U-I colour according to TERAMO Models (Raimondo et al. 2005) for 11 and 13 Gyr old single stellar populations. The solid red line indicates the adopted piecewise linear approximation that we adopt for the transformation from U-I to [Fe/H] in this paper, see equations 1 and 2.

We note that a polynomial fit is problematic for the extrapolation to colours bluer than the model limits at  $U-I \lesssim 1.55$  mag ( $[Fe/H] \lesssim -1.8$  dex), which is why we preferred a piecewise linear approximation of the models.

The resulting data points in mass-metallicity space are shown in Fig. 7 for both Hydra and Centaurus along with a linear fit to

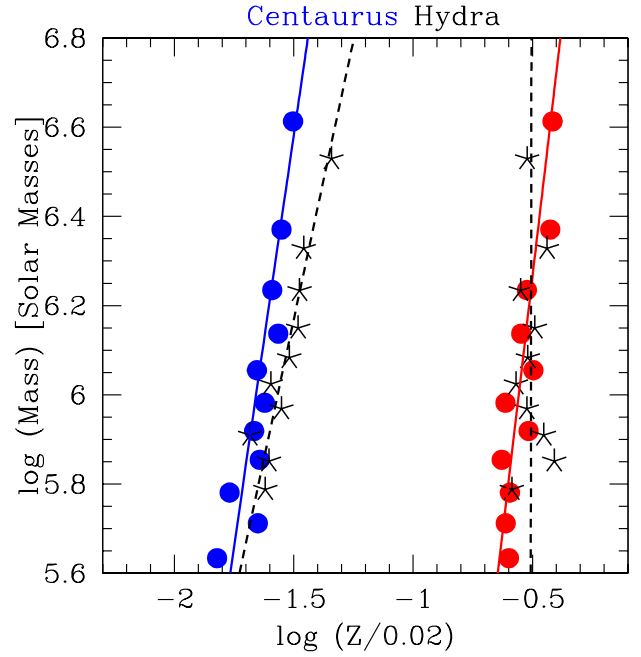


**Fig. 7.** Mass-metallicity relations of GCs in Centaurus and Hydra, as converted from the UI colour magnitude relations shown in Fig. 5. Centaurus is shown in blue/red filled circles, Hydra in black asterisks. Lines indicate unweighted linear fits to the data.

the data. The slopes of the linear fits are listed in Table 1 in terms of the exponent  $\alpha$  in  $Z \propto M^\alpha$ . In particular we find  $Z \propto M^{0.27 \pm 0.05}$  for GCs in Centaurus and  $Z \propto M^{0.40 \pm 0.06}$  for GCs in Hydra along the blue sequence.

## 4. Discussion

In this Section we compare our findings to predictions of the self-enrichment model of Bailin & Harris (2009). This includes a detailed discussion of how our findings can be used to constrain GC mass and radius evolution and primordial star formation efficiencies in the context of that model.

### 4.1. The default model parameters of Bailin & Harris (2009)

Both in Strader & Smith (2008) and Bailin & Harris (2009) self-enrichment scenarios of star clusters are discussed with a focus on the blue tilt. The basic idea of self-enrichment is simple. Self-enrichment (by SNII ejecta) starts to become efficient when the gravitational binding energy ( $\propto$  mass) of and gas ram pressure within the primordial cluster becomes comparable to the kinetic energy output of SNII. In the following detailed discussion we focus on the more recent model of Bailin & Harris.

To calculate the resulting metallicity in a globular cluster as a consequence of self-enrichment, Bailin & Harris used as factor of parametrisation the metal-retention fraction  $f_Z$ , which is obtained from the competition between SNII kinetic energy output gravitational potential, (equation 28 of their paper):

$$f_Z = e^{-\frac{f_\star E_{SN} r_t}{10^2 M_\odot G M_C}} \quad (3)$$

This expression is valid for a density profile of an isothermal sphere ( $\rho \propto r^{-2}$ ).  $f_\star$  denotes the star formation efficiency,

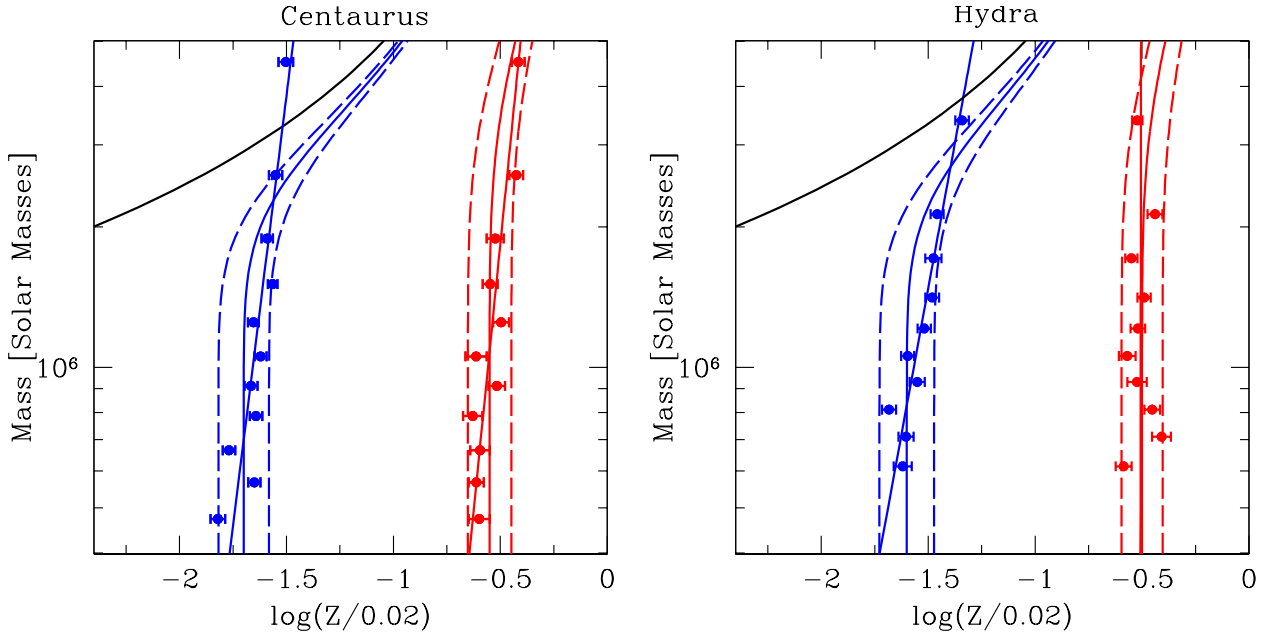


**Fig. 8.** Comparison between the measured mass-metallicity data points of GCs in Hydra/Centaurus, and the default version of the self-enrichment model by Bailin & Harris. The Y axis is the current mass of the GCs. The black curve shows the self-enrichment model with  $\beta = 2$  and  $f_* = 0.3$ . The blue and red solid curves are the result of the combination between self-enrichment and pre-enrichment. The dashed lines represent the scatter in colour of the points used in Fig. 5, converted into metallicity. The straight lines are the linear fits from Fig. 7.

i.e. the fraction of primordial gas that is converted to stars.  $E_{SN} = 10^{51}$  ergs is the typical energy released by one SN II,  $M_C$  is the mass of the proto-cluster cloud, and  $r_t$  is the truncation radius, which is identified with the half-light radius  $r_h$  in the following (see also Mieske et al. 2010). The factor  $10^2$  in the denominator of the exponent comes from the fact that (for a Salpeter/Kroupa type high-mass IMF) about one SN is formed per 100 solar masses formed in stars (Fig. 3 of their paper). For  $\beta \neq 2$ , one obtains  $f_Z$  (equation 36 of their paper):

$$f_Z = \left(1 - \frac{f_*^2 E_{SN} r_h (2 - \beta)}{10^2 M_C G M_{GC}}\right)^{\frac{3-\beta}{2-\beta}} \quad (4)$$

Both  $f_Z$  and  $f_*$  are then used as scaling factor in the following basic equation describing the final cluster metallicity  $Z_C$  obtained by including self-enrichment (equation 7 of Bailin & Harris):

$$\log_{10}\left(\frac{Z_C}{Z_\odot}\right) = 0.38 + \log_{10}(f_* f_Z) + \log_{10}\left(\frac{Z_{pre}}{Z_\odot}\right) \quad (5)$$

where 0.38 is adopted from previous studies (Woosley et al. 1995 and Nomoto et al. 1997).  $Z_{pre}$  is the pre-enrichment of the globular cluster, i.e. the average metallicity of its first generation of stars. In their default model, Bailin & Harris assume  $f_* = 0.3$ ,  $r_h = 1$  pc, and an isothermal sphere with  $\rho \propto r^{-2}$ .

In Fig. 8 we overplot the model predictions using the above default parameters to our data for Hydra and Centaurus. The only parameter that is undefined in this case is the pre-enrichment level  $Z_{pre}$ . We find that values of  $\log_{10}(Z_{pre}/Z_\odot) = -1.70$  and  $-0.55$  for Centaurus and  $-1.60$  and  $-0.50$  for Hydra give the lowest deviation between the model and the data.

The default model in Fig. 8 does not agree well with our data. The predicted (model) slope for high mass GCs is too

strong. Furthermore, the continuation of the mass-metallicity relation towards lower masses as found by the data is not predicted by the model. A similar conclusion was found in Mieske et al. (2010) based on the blue tilt measurement for the Fornax and Virgo clusters from HST data. In that article we show that the tilt becomes notable one order of magnitude in mass below the on-set mass expected by the above default self-enrichment model. With the present (ground-based) data we thus confirm this finding in a different environment.

In this context one should not forget that self-enrichment takes place very early in the evolution of a star clusters. It is assumed to happen after the explosion of the most massive stars, when their ejecta cools down and pollutes the material of forming stars. This happens approximately 5 Myr after the beginning of the stellar formation process (Bailin & Harris 2009). It is crucial for the model that the pollution of the ISM by SN ejecta occurs before the bulk of (lower-mass) stars is formed.

It is thus important for the input parameters of the self-enrichment model to represent as accurately as possible the *initial conditions of the clusters*. Turning the argument around, comparing predictions of self-enrichment models to actual data allows us to constrain the initial star formation conditions in globular clusters. In particular, mass loss and the mass-radius relation of primordial GCs are very important in shaping the present-day observed mass-metallicity relation. We will discuss this in detail in the next two subsections.

## 4.2. Inclusion of GC mass and radius evolution into the model

### 4.2.1. Mass Loss

During its life time, a globular cluster will undergo mass loss due to stellar and dynamical evolution (e.g. Lamers et al. 2005



& 2010, Kruijssen 2009). This accumulated mass loss has two effects.

A) Based on the present-day mass as known from observations, the accumulated mass loss determines the primordial stellar cluster mass after star formation had finished. This primordial mass is the value to be adopted as globular cluster mass  $M_{GC}$  in equation 4. We reiterate that the mass of the cluster's progenitor gas cloud is still higher than this by a factor of  $1/f_*$ , with  $f_*$  being the star formation efficiency at the time of cluster formation (equation 4).

B) Preferential loss of late dwarf stars – i.e. after dynamical relaxation timescales – changes the integrated colour of a cluster.

ad A.1) Regarding stellar evolution (winds, ejecta), it is well established that between 40% and 60% of the mass of the cluster is lost after 12 Gyr (e.g. Kruijssen et al. 2008, Sippel et al. 2012) because of this. We adopt a representative mass loss of 50% in the following.

ad A.2) Mass loss due to dynamical evolution occurs when stars located in the outskirts of a cluster become unbound, because of their proper motion and tidal influence of their host galaxy (e.g. Baumgardt & Makino 2003, Sippel et al. 2012). Observational studies have shown that the total dynamical mass loss experienced by a cluster can approximately be considered as mass-independent (Jordan et al. 2007; see also Kruijssen 2009). Theoretical arguments also predict only a weak dependence of mass loss *rate* on the total cluster mass:

$$\frac{dM}{dt} = \frac{M(t)^{(1-\gamma)}}{t_0} \quad (6)$$

with  $\gamma \sim 0.8$  (Lamers et al. 2010). Across a factor of ten in present-day mass, the theoretically expected accumulated mass loss would thus vary by only  $\pm 30\%$  around the mean. The typical accumulated mass loss for globular clusters over a Hubble time ranges from  $3$  to  $5 \times 10^5 M_\odot$  (Jordan et al. 2007). We thus adopt an accumulated dynamical mass loss of  $\Delta = 4 \times 10^5 M_\odot$  in the following, independent of GC present-day mass.

Combining the effects of dynamical and stellar evolution mass loss, we thus obtain the following relation between present-day mass  $M_t$  and mass at self-enrichment  $M_0$ .

$$M_0 = \frac{M_t + 4 \times 10^5}{0.5} [M_\odot] \quad (7)$$

We note that the timescales of both contributors are quite different: stellar evolution mass loss occurs very quickly in the early stages of a cluster's life, while dynamical mass loss happens on very long timescales comparable to a Hubble time (e.g. Sippel et al. 2012).

ad B) Recent studies investigated the effect of this dynamical dissolution of star clusters on their integrated colours (Kruijssen & Lamers 2008, Anders et al. 2009). These studies predict star cluster colours at a determined age and metallicity as a function of the ratio  $t_{dyn}$  between the current age and the dissolution time. It was shown that colour changes start to set in after  $\approx 0.4$  dissolution time. Qualitatively, this happens because after sufficient dynamical evolution, preferred stellar types are evaporated, namely late-type dwarfs. This in turn changes the colour of the stellar population bluewards (see also Mieske et al. 2010).

We express  $t_{dyn}$  as (Jordan et al. 2007, Mieske et al. 2010):

$$t_{dyn} = 1 - \frac{M_{GC}}{M_{GC} + \Delta} \quad (8)$$

This allows us to calculate the colour change at each luminosity bin, adopting the predictions by Kruijssen & Lamers (2008) in the V,I bands as a function of  $t_{dyn}$ . For the present study we then convert this to (U-I) colours with  $\frac{d(V-I)}{d(U-I)} = 3.5$ . This slope between both colours is derived from the subset of our data which has U,V,I coverage.

#### 4.2.2. Mass-Radius Relation

Bailin & Harris (2009) adopted for their default model a mass independent half-light radius  $r_h$  of 1 parsec, smaller than present-day average radii of 3 pc due to the early expansion after gas removal (e.g. Baumgardt & Kroupa 2007). The assumption of a mass-independent primordial GC radius may, however, be too simple, as suggested by Gieles et al. (2010). These authors argue that a primordial mass-radius relation down to low GC masses is dynamically more plausible. We will thus investigate how the predictions for the self-enrichment model change between a fixed radius and a mass radius relation for the GCs at time of self-enrichment. For the latter we adopt from Gieles et al. (2010):

$$\log\left(\frac{r_h}{1 \text{ pc}}\right) = -3.63 + 0.615 * \log\left(\frac{M_0}{M_\odot}\right) \quad (9)$$

where  $r_h$  and  $M_0$  are the half-mass radius and mass at time of self-enrichment. This relation is displayed in Figure 9. With the given offset -3.63, one obtains a radius of 3 pc for a  $2 \times 10^6 M_\odot$  mass cluster (Bailin & Harris 2009). In Fig. 9 we also indicate in green an approximation for the present-day mass radius relation of GCs (e.g. Gieles et al. 2010, Mieske et al. 2006, Murray 2009): a piecewise function with a mass-independent radius of 3 pc for  $M < 2 \times 10^6 M_\odot$ , and a mass-radius relation according to equation 9 for  $M > 2 \times 10^6 M_\odot$ . The blue line in Fig. 9 indicates the fixed  $r_h = 1$  pc adopted by Bailin & Harris (2009).

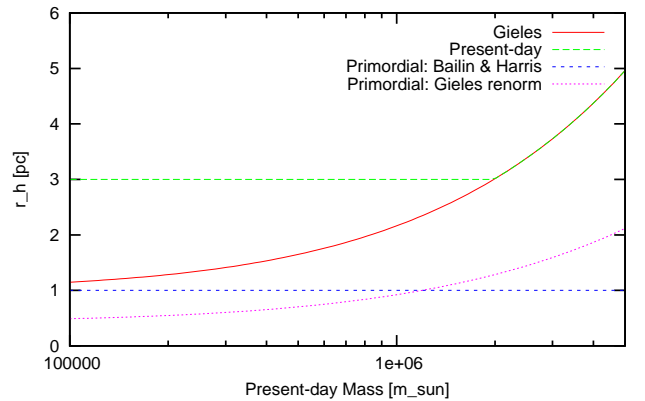


**Fig. 9.** **Red:** Star cluster mass -  $r_h$  relation from Gieles et al. (2010), normalised to have  $r_h=3$ pc at a mass of  $2 \times 10^6 M_\odot$ . **Green:** present-day mass-radius relation (e.g. Mieske et al. 2006, Gieles et al. 2010): star clusters have a mass-independent half-light radius for masses below  $2 \times 10^6 M_\odot$ , and a mass-radius relation above that mass. **Blue:** Primordial mass-radius relation (constant radius) adopted by Bailin & Harris (2009) for star clusters at time of self-enrichment. **Magenta:** Primordial mass-radius relation adopted by renormalising the red (Gieles) curve to a mean of  $r_h = 1$  pc in the observed GC mass range  $[5 \times 10^5 : 4 \times 10^6] M_\odot$ . We note that the x-axis is the present-day mass, which is converted to original mass according to equation 7.

### 4.3. Best fitting models

#### 4.3.1. Constant vs. mass-dependent radius

Equations 4 and 5 show that the determining parameters of the self-enrichment efficiency of a cluster are: the star formation efficiency  $f_*$ , the mass-radius relation, the density profile  $\rho \propto r^{-\beta}$  and the pre-enrichment level. Here we aim at constraining these parameters with our data.

In Fig. 10 we fit the modified model discussed in the previous subsection to the data. Compared to the default model shown in Fig. 8, we keep the surface density distribution of an isothermal sphere ( $\beta = 2$ ), and adopt the following modifications for the other parameters:

- Top panels (left Centaurus, right Hydra): dynamical and stellar evolution mass loss is included according to equation 7. As in the default model, a mass-independent primordial half-light radius of  $r_h = 1$  pc is assumed. Then we vary the *star formation efficiency* and *pre-enrichment levels* to obtain the best-fit of the model to the data, using least-squares minimisation. We find best-fit star formation efficiencies of 0.65 for Centaurus and 0.50 for Hydra and pre-enrichment values of (-1.65, -0.55) for Centaurus and (-1.55, -0.50) for Hydra. The rms difference between model and data [Fe/H] is 0.031 dex for Centaurus and 0.028 dex for Hydra.
- Bottom panels (left Centaurus, right Hydra): as in the top panels, dynamical and stellar evolution mass loss is included according to equation 7. In contrast to the top panel, we now adopt a mass-radius relation as in equation 9, normalised to a mean  $r_h = 1$  pc across the considered GC mass range [ $5 \times 10^5 : 4 \times 10^6$ ]  $M_\odot$ . We find best-fitting star formation efficiencies of 0.42 for Centaurus and 0.36 for Hydra, and pre-enrichment values of (-1.70, -0.55) for both Centaurus and Hydra. The rms difference between model and data [Fe/H] is 0.020 dex for Centaurus and 0.10 dex for Hydra.

From Fig. 10 one notes that the introduction of a (physically well motivated) mass-radius relation leads to a better fit to the data, and also to more realistic star formation efficiencies. The rms between model and data is reduced by about a factor of two when including the mass-radius relation (bottom panel of Fig. 10). With a mass-radius relation at an average  $r_h$  of 1 pc, self-enrichment sets in at lower masses but increases less rapidly towards larger masses, when compared to a mass-independent  $r_h = 1$  pc.

#### 4.3.2. Degeneracy between radius, star-formation efficiency, surface density profile, pre-enrichment level

In Fig. 11 we provide a more general overview of the degeneracy between self-enrichment model parameters average radius, star-formation efficiency, surface density profile, and pre-enrichment level. All figures assume the mass-radius relation in equation 9 normalised to a mean radius within the range [ $5 \times 10^5 : 4 \times 10^6$ ]  $M_\odot$  as given on the x-axis. We first discuss the face-value constraints obtained by the model fits, and then add physically motivated constraints to several model parameters.

The top panels plot the best fitting star formation efficiency as a function of average  $r_h$  and for a range of surface density profile parameter  $\beta = [2.0; 2.2]$ . The star formation efficiency required to match the data decreases with increasing radius, and increases with increasing  $\beta$ . These trends become clear in the context of the self-enrichment scenario: a lower star formation effi-

ciency results in a larger primordial cluster mass at fixed present-day mass, and thus a deeper potential well. Self-enrichment was thus more efficient at a given present-day mass for lower primordial star formation efficiency. At the same time, a larger primordial radius gives a weaker primordial self-enrichment at a fixed present-day mass given the resulting shallower potential well. Finally, a steeper surface density profile (larger  $\beta$ ) gives a deeper potential well and thus a stronger self-enrichment.

The bottom panels show the best fitting pre-enrichment level as a function of average  $r_h$  and for a range of surface density profile parameter  $\beta = [2.0; 2.2]$ .

In both the upper and lower panels, the rms of the data around the models vary by  $\leq \pm 20\%$  among the various model flavours, significantly less variation than the factor of two difference in rms to the model flavour with a fixed primordial radius. That is, changing from a fixed radius to a mass-radius relation is the most important model update.

For Hydra all plotted models span a total range of [0.007; 0.009] dex in rms between data and models. This very small range of  $\pm 10\%$  shows that no combination of the three model parameters is strongly preferred. For Centaurus the variation in rms between model flavours is somewhat larger with  $\pm 20\%$  and a range of [0.014; 0.022]. Best-fitting models are those at large  $\beta$ , i.e. very steep initial surface density profile. At a fixed  $r_h = 1$  pc, the rms is 0.020 for  $\beta = 2.0$  and 0.015 for  $\beta = 2.2$ . At a given  $\beta$ , models with smallest  $r_h = 0.5$  pc have about 20% higher rms than models with the largest  $r_h = 3.5$  pc.

Given the quite moderate distinction in rms between the various best-fitting model flavours in Fig. 11, it is appropriate to consider physically motivated boundary conditions for the model parameters.

**1. Pre-enrichment level:** The somewhat low values of formally possible pre-enrichment levels down to [Fe/H]  $\sim -1.9$  for Hydra) in Fig. 11 are found because our data are restricted to GCs brighter than the turn-over magnitude. The data allow reasonable model fits for the case that self-enrichment sets in at masses lower than our faint luminosity limit. The model curves would in this case not straighten out at the cutoff mass of our investigation, but continue to extend towards lower metallicities for lower masses. To avoid the fitting degeneracy due to this extrapolation, we consider the well-known metallicity distribution of GCs in the Milky Way as an anchor point for the pre-enrichment level. According to the catalogue of Harris et al. (1996), the median metallicity of the metal-poor GC population in the Milky Way is about [Fe/H] = -1.6 dex. Allowing for a U-I colour scale uncertainty of 0.10 mag in our data (see Sect. 2.2.1) and taking into account the slope of  $\sim 2$  between [Fe/H] and U-I (equation 1), we thus adopt a pre-enrichment lower limit of [Fe/H] = -1.8 dex. This excludes for the Hydra cluster models that have average  $r_h > 2$  pc and surface density profiles steeper than  $\beta = 2.1$ . For the Centaurus cluster, this restriction of pre-enrichment level to  $\leq -1.8$  dex does not constrain the range of fitting models.

**2. Star formation efficiency:** It is widely assumed that star formation efficiency even in dense cores of molecular clouds is  $\leq 0.3$  (e.g. Lada & Lada 2003). We thus adopt a conservative upper limit of  $f_* \leq 0.4$ .

**3. Primordial half-light radius:** the typical present-day half-light radii of most globular clusters are  $\sim 3$ -3.5 pc (e.g. Jordan et al. 2005). At the same time, primordial cluster expansion due to gas expulsion increases the half-light radius by at least a factor of 2 (Baumgardt & Kroupa 2007, Gieles et al. 2010 Fig. 2). We thus adopt a (still conservative) upper limit of  $r_h \lesssim 2$  pc.

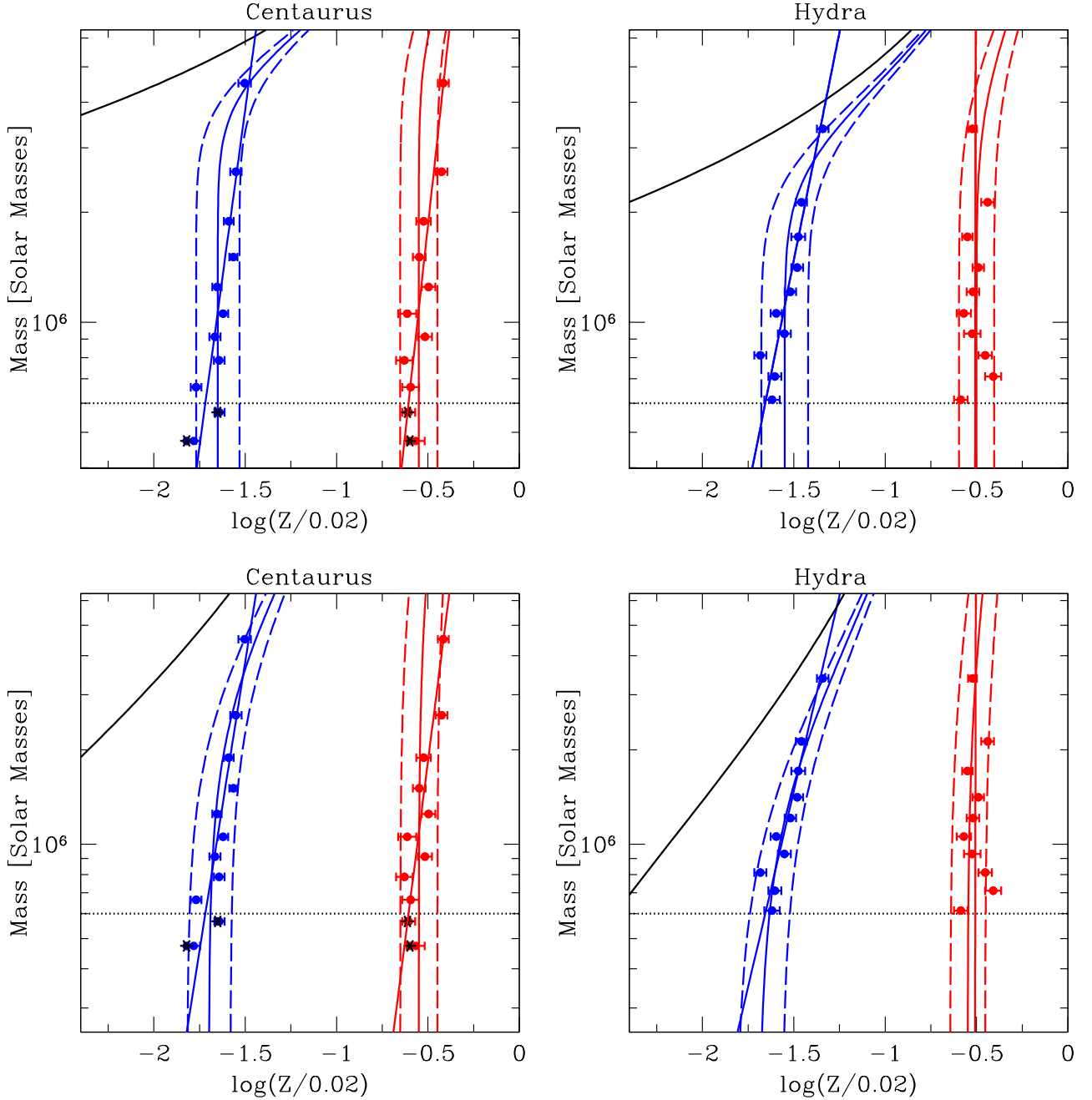


**Fig. 10.** Model fits to our mass-metallicity data. **Left:** Centaurus; **Right:** Hydra. Compared to the model in Fig. 8, we include stellar evolution mass loss and dynamical mass loss according to equation 7, and then determine the best-fitting star formation efficiency. The dotted horizontal line represents the critical mass below which the clusters will undergo colour changes due to dynamical mass evolution. Below this line, asterisks indicate the data points without colour changes. **Top panels:** Primordial half-light radius  $r_h$  is fixed at 1 pc. We find best-fit star formation efficiencies of 0.65 for Centaurus and 0.50 for Hydra and pre-enrichment values of (-1.65,-0.55) for Centaurus and (-1.55,-0.50) for Hydra. **Bottom panels:** The mass-radius relation as in equation 9, normalised to a mean  $r_h=1$  pc across the GC present-day mass range [ $5 \times 10^5 : 4 \times 10^6$ ]  $M_\odot$ . We find best-fitting star formation efficiencies of 0.42 for Centaurus and 0.36 for Hydra, and pre-enrichment values of (-1.70,-0.55) for both Hydra and Centaurus.

For the Hydra cluster, the above physical constraints restrict the models to an isothermal sphere – or only slightly steeper profile – and a primordial radius  $r_h$  in the range [1:2] pc, corresponding to a range in  $f_\star$  of [0.36:0.24]. The upper limit in radius translates to the lower limit of  $\sim 0.24$  in  $f_\star$ , and analogously the lower radius limit comes from the imposed upper limit of  $f_\star$ .

For the Centaurus cluster, the star formation efficiency and the  $r_h < 2$  limit constrain the models (not so the limit on pre-

enrichment). This restricts the models to a range of [1.5:2] pc and an isothermal sphere, with a corresponding  $f_\star$  range [0.32:0.27].

From Fig. 11 it also becomes clear that the steeper blue tilt for Hydra in comparison to Centaurus can be explained either by a  $\sim 30\%$  smaller average  $r_h$  in Hydra at fixed  $f_\star \sim 0.3$ , or analogously by a  $\sim 20\%$  smaller  $f_\star$  at fixed  $r_h \sim 1.5$  pc.

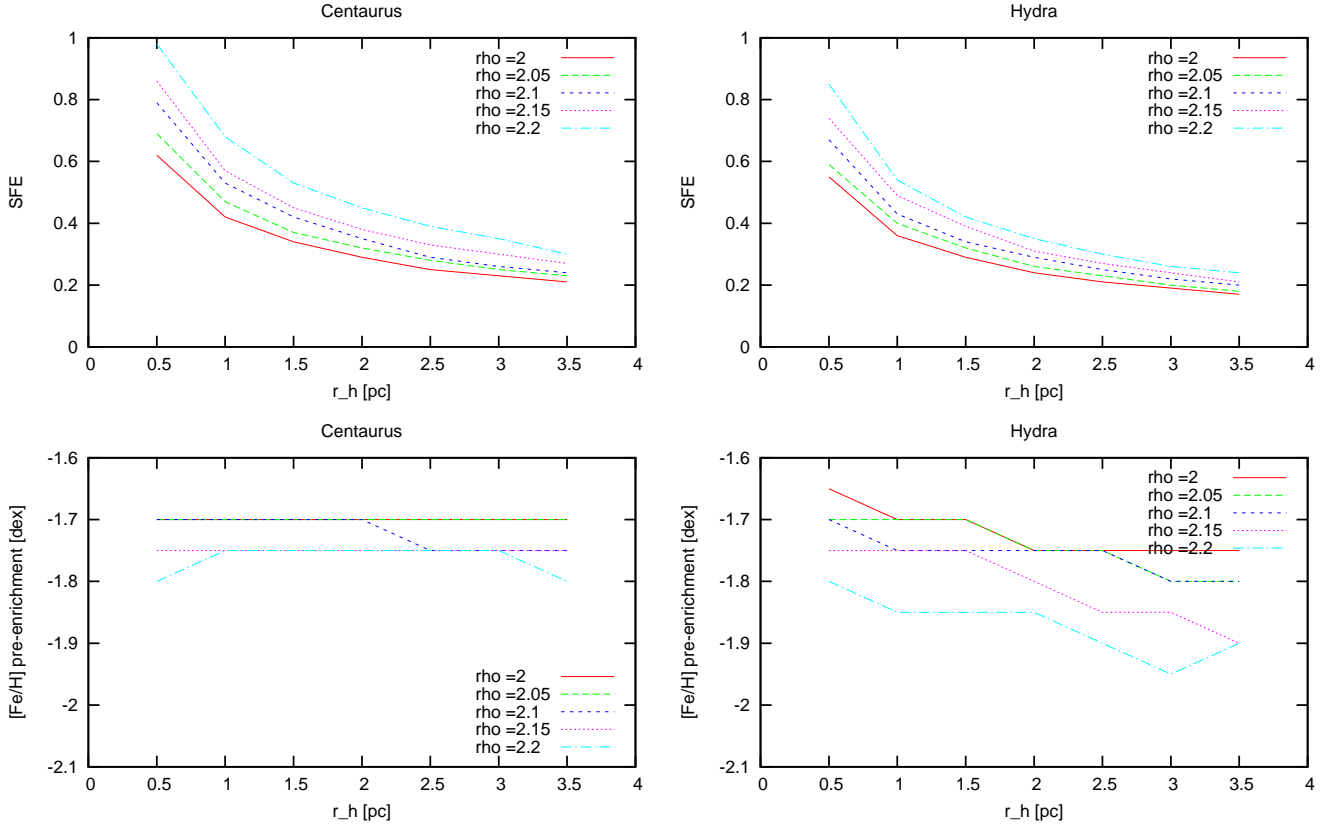


**Fig. 11.** **Top:** Best fitting star formation efficiency  $f_*$  for the given mean radius  $r_h$  and surface density profile slopes  $\beta$ . Primordial boundary conditions as discussed in the text would imply  $f_* \lesssim 0.4$  and  $r_h \lesssim 2$  pc. **Bottom:** Best fitting pre-enrichment level for the same range in mean radius  $r_h$  and surface density profile slopes  $\beta$  as above. A physically motivated lower limit for the pre-enrichment level is about  $\sim -1.8$  dex, see text for details.

#### 4.4. Difference between Centaurus and Hydra

It was shown above that the amplitude of the blue tilt in Hydra is slightly stronger than in Centaurus, see Table 1 and Fig. 7. The slope  $\gamma = d(U - I)/dI$  is  $-0.081 \pm 0.012$  for Hydra and  $\gamma = -0.057 \pm 0.011$  for Centaurus, which formally is a  $1.5\sigma$  level difference.

To investigate this in more detail, we show in Fig. 12 the cumulative radial distribution of GC candidates in both Hydra and Centaurus, centered on NGC 3311 and NGC 4696 respectively. It is clear from this figure that the GC distribution is more centrally concentrated for Hydra than for Centaurus. We note that this is imposed mainly by the observational setup (Fig. 2), which was focused on NGC 3311 in Hydra, whereas the Centaurus observations focused on the area between the central galaxy NGC 4696 and NGC 4709. The median projected distance to NGC 3311 for the Hydra GCs is about 25 kpc, while the median distance to NGC 4696 for the Centaurus GCs is about 42 kpc. The difference becomes even more pronounced when comparing this to the respective effective radii of both central galaxies determined from the V-band FORS data (Misgeld et al. 2008 & 2009). The effective radius of the Centaurus cluster central galaxy NGC 4696 is  $82''$  or 17 kpc, while for the Hydra central galaxy NGC 3311 it is  $150''$  and thus 35 kpc. Thus the galaxy half-light radius in Hydra comprises  $2/3$  of all GCs, but only 10% of the Centaurus GCs in our data set.

A uniform area coverage in both clusters would be needed to tell whether the GC density profiles are intrinsically different, or, whether this higher concentration in Hydra is entirely due to the

different spatial coverage of the existing data. Analogously, such a uniform area coverage would help to corroborate the formally significant red tilt observed in Centaurus, i.e. the non-zero slope in the red sequence. A significant red tilt is generally not seen in other environments (e.g. Table 1 and Harris et al. 2009a). Given our lacking coverage in the central Centaurus field, the red sequence is only sparsely populated and thus the red tilt for Centaurus would need to be confirmed with more photometric coverage in the cluster center.

In Mieske et al. (2010) it was shown that within the joint Fornax and Virgo cluster GC system, the blue tilt is more pronounced for GCs at smaller projected radii from their host galaxies. One may thus ask the question whether the weaker tilt in Centaurus is related to its less centrally concentrated GC sample compared to Hydra. As mentioned above for the Centaurus sample the median projected distance to the central galaxy NGC 4696 is about 42 kpc. Adopting such a limit of 42 kpc between inner and outer sample, the inner slope is  $\gamma = -0.061 \pm 0.016$ , and the outer slope is  $\gamma = -0.045 \pm 0.018$ , marginally shallower than the inner sample. Similarly for Hydra, with a limit of 25 kpc between inner and outer sample, the inner slope is  $\gamma = -0.061 \pm 0.016$ , and the outer slope is  $\gamma = -0.045 \pm 0.018$ . This qualitatively confirms the finding in Mieske et al. (2010) that the blue tilt is stronger at smaller cluster centric distance. The difference between the inner Centaurus slope and overall Hydra slope is insignificant, and the formally lowest difference is found between the inner Centaurus and outer Hydra sample ( $-0.061$  vs.  $-0.068$ ). As noted in the previous subsection, a spa-

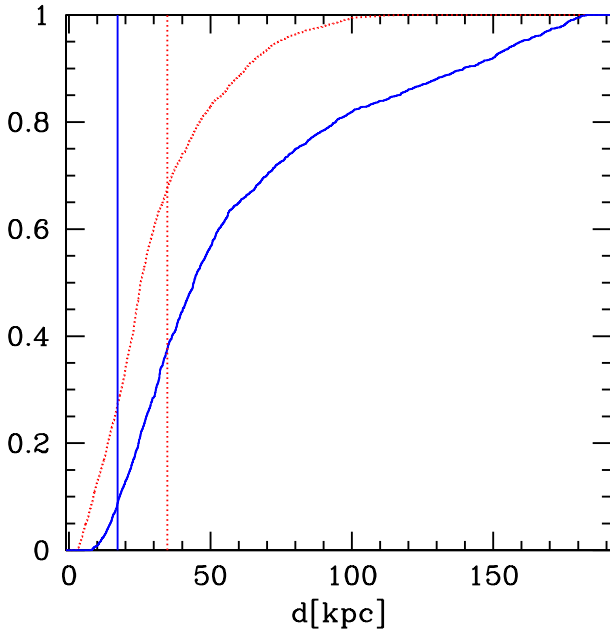


**Fig. 12.** Cumulative radial distribution of GC candidates in Hydra (dotted red line) and Centaurus (solid blue line) around the central galaxies NGC 3311 and NGC 4696, respectively. We note the more central concentration of the Hydra GCs which is imposed by the observational setup, see also Fig. 2. We furthermore indicate as vertical lines the effective radii of the respective central galaxies.

tial variation in self-enrichment efficiency can be explained by a corresponding variation in primordial star formation efficiency or cluster radius.

In concluding we reiterate that in this study we assume a co-eval sample of old globular clusters with luminosity weighted ages around a Hubble time. In future studies it would be worthwhile to address to which extent the presence of young-to-intermediate age GCs may influence the measured blue tilt, in particular its spatial variation.

#### 4.5. Comparison to the Milky Way Globular Clusters

It is interesting to check whether the self-enrichment model proposed to explain the blue tilt is consistent with what is observed in GCs of our own Milky Way.

As noted earlier on, the cluster-to-cluster variation in  $[\text{Fe}/\text{H}]$  is always superposed on the effect of  $[\text{Fe}/\text{H}]$  increase due to self-enrichment within individual clusters. The statistical significance of the trend is between  $7\text{--}10\sigma$  in our large samples of about 2500 GCs in each environment. In the Milky Way there are only about 50 GCs in the same absolute magnitude range (Harris et al. 1996). It is thus clear that no significant blue tilt is expected to be notable in the Milky Way (see also Strader et al. 2009), since the GC-to-GC scatter in mean  $[\text{Fe}/\text{H}]$  supersedes the smooth and slow effect of self-enrichment.

However, the *width of the stellar  $[\text{Fe}/\text{H}]$  distribution* within individual globular clusters is a much more direct tracer of possible self-enrichment. The typical width  $\sigma$  of the  $[\text{Fe}/\text{H}]$  distribution in lower-mass GCs of the Milky Way is about 0.03 dex, see Fig. 1 of Willman & Strader (2012). Then, for the most massive GCs like Omega Centauri and M54, this  $[\text{Fe}/\text{H}]$  width increases notably to about 0.2 dex. Such broad  $[\text{Fe}/\text{H}]$  distributions, which are also seen in dwarf spheroidals, have often been interpreted as

results of self-enrichment. An interesting question in this context is whether the broadened metallicity distribution for GCs like Omega Centauri (Johnson & Pilachowski 2010) is naturally explained within a self-enrichment scenario of star clusters. Or, whether such strong self-enrichment as observed in Omega Centauri implies that it was once embedded in a much more massive halo (e.g. Hilker & Richtler 2000, Gnedin et al. 2002). See for this also the discussion in Willman & Strader (2012).

For comparing our best-fit self-enrichment models to the GCs in the Milky Way, we thus convert the model predictions of mean  $[\text{Fe}/\text{H}]$  to a predicted width of the stellar  $[\text{Fe}/\text{H}]$  distribution. Such a conversion can be very complex since individual enrichment histories are variable – in the Bailin & Harris model, the metallicity spread is generated by the range of formation times of the low-mass stars, which are a few Myrs. Here we adopt a simple approach of defining the expected width  $\sigma_{[\text{Fe}/\text{H}]}$  of the stellar  $[\text{Fe}/\text{H}]$  distribution as being equal to the difference between the model predicted  $[\text{Fe}/\text{H}]_{\text{enrich}}$  and the pre-enrichment level  $[\text{Fe}/\text{H}]_{\text{pre-enrich}}$ , including a minimum floor of 0.03 dex.

$$\sigma_{[\text{Fe}/\text{H}]} = \sqrt{([\text{Fe}/\text{H}]_{\text{enrich}} - [\text{Fe}/\text{H}]_{\text{pre-enrich}})^2 + 0.03^2} \quad (10)$$

It is important to keep in mind that the model predicted  $[\text{Fe}/\text{H}]_{\text{enrich}}$  is very close to the  $[\text{Fe}/\text{H}]$  derived from the actual data of the Centaurus/Hydra GCs. In Fig. 13 we compare the predicted  $\sigma_{[\text{Fe}/\text{H}]}$  for both the Centaurus (blue) and Hydra (red) best-fit models for a mean  $r_h = 1$  (fat lines) and  $r_h = 1.5$  pc (thin lines) to the  $\sigma_{[\text{Fe}/\text{H}]}$  observed in Milky Way GCs (Willman & Strader 2012). Two things can be noted.

1. The best-fit Centaurus model fits the Milky Way distribution quite well, though being slightly below the Milky Way values. For  $r_h = 1$  pc the sharp rise of  $\sigma_{[\text{Fe}/\text{H}]}$  around  $M_V = -9.5$  mag to values around 0.1–0.2 dex in the luminosity range of omega Centauri and M54 is reproduced well. The (stronger) Hydra blue tilt implies a larger  $\sigma_{[\text{Fe}/\text{H}]}$  slightly above to what is seen in the Milky Way. We note that the only difference at  $r_h = 1$  pc between the Hydra and Centaurus models is the star formation efficiency: 0.42 for Centaurus and 0.36 for Hydra (see Fig. 10).

2. The curves for  $r_h = 1$  pc imply a smaller  $\sigma_{[\text{Fe}/\text{H}]}$  spread than the curves at  $r_h = 1.5$  pc. This is because a larger primordial radius requires a lower pre-enrichment level to fit the data, and thus the measured metallicities at high masses are farther away from the pre-enrichment levels. In this context we note that *at the same* pre-enrichment level, variations in  $r_h$  and star formation efficiency are degenerate as already mentioned above. For example, the bold curve for Centaurus can be represented both by combination of an average primordial radius  $r_h = 1$  pc and SFE=0.42, *and* an average primordial radius  $r_h = 3$  pc and SFE=0.23. The latter example may fit better the case of omega Centauri with its present day  $r_h = 8$  pc.

The above example shows that broadened metallicity distributions like found in some massive MW globular clusters may be natural consequences of cluster self-enrichment processes, without the need to invoke an additional embedding in a more massive halo (e.g. a dwarf galaxy) at time of formation (e.g. Dinescu et al. 1999, Majewski et al. 2000, Gnedin et al. 2002, Bekki et al. 2006).

One caveat is that the self-enrichment model applied here (Bailin & Harris 2009) assumes quasi-instantaneous reprocessing of SNII ejecta, i.e. on timescales that are short compared to dynamical timescales. This is a simplifying assumption that would need to be elaborated in further detail, given that an age spread of several billion years has been reported for the stellar populations of omega Centauri (e.g. Hilker et al. 2004).



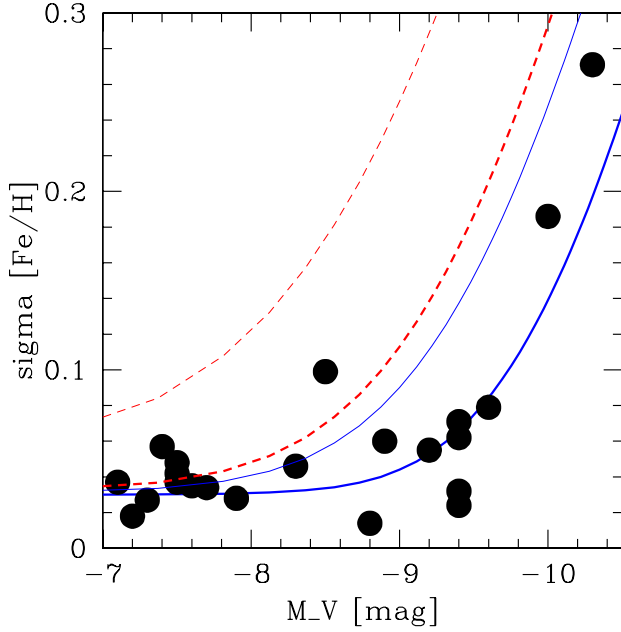


**Fig. 13.** Filled circles indicate the width  $\sigma_{[\text{Fe}/\text{H}]}$  of the stellar metallicity distribution in Galactic GCs plotted vs. their absolute visual magnitude  $M_V$ , compiled from Willman & Strader (2012) & da Costa et al. (2014). The blue curve indicates the width  $\sigma_{[\text{Fe}/\text{H}]}$  predicted from the best-fitting self enrichment model of the Centaurus cluster GCs, the red (dashed) curve represents the predictions from the best-fit model of the Hydra cluster GCs. The bold curves correspond to average primordial  $r_h = 1$  pc, the finer ones to  $r_h = 1.5$  pc.

## 5. Summary and Conclusions

We analyse the colour-magnitude relation of globular clusters (the ‘blue tilt’) in the central 100 kpc of the Hydra and Centaurus galaxy clusters. This analysis is based on deep FORS1 photometry in the U and I bands, which provides a very broad wavelength baseline and thus high metallicity sensitivity. The final sample comprises about 2500 GC candidates in each cluster down to  $M_I \sim -9$  mag, half a magnitude brighter than the GC luminosity function turnover.

We obtain the following results

- In both clusters we measure a significant ‘blue tilt’, i.e. a colour-magnitude relation for the blue globular cluster sub-population. We find  $\gamma = d(U - I)/d(I) = -0.057 \pm 0.011$  for Centaurus and  $\gamma = -0.081 \pm 0.012$  for Hydra. We confirm previous findings that the blue tilt already sets in at present-day masses well below  $10^6 M_\odot$ .
- We convert colours and luminosities to mass and metallicity using TERAMO models (Raimondo et al. 2005), assuming old GC ages of 11-13 Gyrs. We thus obtain a mass-metallicity scaling of  $Z \propto M^{0.27 \pm 0.05}$  for Centaurus and  $Z \propto M^{0.40 \pm 0.06}$  for Hydra. This is the same range than found in previous literature measurements of the GC mass-metallicity scaling, investigating different environments and mostly using HST data.
- We compare the measured mass-metallicity dependence of GCs on star cluster self-enrichment model predictions using the model of Bailin & Harris (2009). To use a realistic

primordial star cluster mass at the time of self-enrichment, we include both stellar evolution and dynamical mass loss effects. We find that the model fits are significantly improved (reducing rms by a factor of two with respect to the data) when assuming a primordial mass-radius relation of star clusters according to Gieles et al. (2010), instead of a fixed, mass independent, cluster radius.

- We investigate and illustrate the degeneracy between model input parameters average radius  $r_h$ , star formation efficiency  $f_\star$ , pre-enrichment level, and surface density profile steepness. The best fit within physically motivated boundary conditions is obtained for  $r_h \sim 1 - 1.5$  pc,  $f_\star \sim 0.3 - 0.4$ , a pre-enrichment level of  $[Fe/H] \sim -1.7$  and a surface density profile of an isothermal sphere. The slightly steeper blue tilt for Hydra can be explained either by a  $\sim 30\%$  smaller average  $r_h$  at fixed  $f_\star \sim 0.3$ , or analogously by a  $\sim 20\%$  smaller  $f_\star$  at fixed  $r_h \sim 1.5$  pc.
- We note that the GC sample in the Centaurus cluster is less centrally concentrated than the Hydra sample, given the observational setup of the observed fields. We show that both in Hydra and Centaurus the blue tilt is stronger for GCs with smaller projected distances to their host galaxies. We thus argue that the slightly stronger tilt in Hydra could be due to its more centrally concentrated GC sample.
- We find that the  $M_V$  vs.  $\sigma_{[\text{Fe}/\text{H}]}$  distribution of Galactic Globular Clusters is consistent with the GC self-enrichment trend observed for the Centaurus cluster.

We conclude that

1. U-I photometry allows us to accurately measure colour-magnitude relation of GCs
2. GC self-enrichment sets in at present-day masses well below  $10^6 M_\odot$
3. The adoption of a primordial mass-radius relation in the self-enrichment model of Bailin & Harris (2009) allows us to fit data very well without requiring non-canonical star formation efficiency, surface density profile, or average radii.
4. The comparison between the blue tilt strength of Hydra and Centaurus supports previous findings of variations of self-enrichment efficiency with cluster-centric distance. Spatial variations of primordial cluster radius or star formation efficiencies can explain such a behaviour.
5. Broadened metallicity distribution like found in some MW globular clusters can be natural consequences of cluster self-enrichment, without the need to invoke an additional embedding in a more massive halo (e.g. a dwarf galaxy) at time of formation.

*Acknowledgements.* We thank the anonymous referee for very constructive comments which helped to improve this paper. JF acknowledges financial support from the ESO Chile Office for Science.

## References

- Anders, P., Lamers, H. J. G. L. M., & Baumgardt, H. 2009, *A&A*, 502, 817
- Ashman, K. M., Bird, C. M., & Zepf, S. E. 1994, *AJ*, 108, 2348
- Bailin, J. & Harris, W. E. 2009, *ApJ*, 695, 1082

- Bassino, L. P., Faifer, F. R., Forte, J. C., et al. 2006, *A&A*, 451, 789
- Baumgardt, H. & Kroupa, P. 2007, *MNRAS*, 380, 1589
- Baumgardt, H., Kroupa, P., & Parmentier, G. 2008, *MNRAS*, 384, 1231
- Baumgardt, H. & Makino, J. 2003, *MNRAS*, 340, 227
- Bedin, L. R., Piotto, G., Anderson, J., et al. 2004, *ApJ*, 605, L125
- Bekki, K. & Norris, J. E. 2006, *ApJ*, 637, L109
- Blom, C., Spitler, L. R., & Forbes, D. A. 2012, *MNRAS*, 420, 37
- Brodie, J. P. & Strader, J. 2006, *ARA&A*, 44, 193
- Bruzual, G. & Charlot, S. 2003, *MNRAS*, 344, 1000
- Cockcroft, R., Harris, W. E., Wehner, E. M. H., Whitmore, B. C., & Rothberg, B. 2009, *AJ*, 138, 758
- Da Costa, G. S., Held, E. V., & Saviane, I. 2014, *MNRAS*
- D’Antona, F., Bellazzini, M., Caloi, V., et al. 2005, *ApJ*, 631, 868
- D’Antona, F., Caloi, V., Montalbán, J., Ventura, P., & Gratton, R. 2002, *A&A*, 395, 69
- D’Ercole, A., Vesperini, E., D’Antona, F., McMillan, S. L. W., & Recchi, S. 2008, *MNRAS*, 391, 825
- Dinescu, D. I., Girard, T. M., & van Altena, W. F. 1999, *AJ*, 117, 1792
- Dirsch, B., Richtler, T., Geisler, D., et al. 2003, *AJ*, 125, 1908
- Forbes, D. A., Spitler, L. R., Harris, W. E., et al. 2010, *MNRAS*, 403, 429
- Forbes, D. A., Spitler, L. R., Strader, J., et al. 2011, *MNRAS*, 413, 2943
- Forte, J. C., Faifer, F., & Geisler, D. 2007, *MNRAS*, 382, 1947
- Gebhardt, K. & Kissler-Patig, M. 1999, *AJ*, 118, 1526
- Gieles, M., Baumgardt, H., Heggie, D. C., & Lamers, H. J. G. L. M. 2010, *MNRAS*, 408, L16
- Gnedin, O. Y., Zhao, H., Pringle, J. E., et al. 2002, *ApJ*, 568, L23
- Goudfrooij, P. & Kruijssen, J. M. D. 2014, *ApJ*, 780, 43
- Harris, W. E. 1996, *AJ*, 112, 1487
- Harris, W. E. 2009a, *ApJ*, 699, 254
- Harris, W. E. 2009b, *ApJ*, 703, 939
- Harris, W. E., Harris, G. L. H., & Alessi, M. 2013, *ApJ*, 772, 82
- Harris, W. E., Spitler, L. R., Forbes, D. A., & Bailin, J. 2010, *MNRAS*, 401, 1965
- Harris, W. E., Whitmore, B. C., Karakla, D., et al. 2006, *ApJ*, 636, 90
- Hilker, M., Kayser, A., Richtler, T., & Willemsen, P. 2004, *A&A*, 422, L9
- Hilker, M. & Richtler, T. 2000, *A&A*, 362, 895
- Humphrey, P. J. 2009, *ApJ*, 690, 512
- Johnson, C. I. & Pilachowski, C. A. 2010, *ApJ*, 722, 1373
- Jordán, A., Côté, P., Blakeslee, J. P., et al. 2005, *ApJ*, 634, 1002
- Jordán, A., McLaughlin, D. E., Côté, P., et al. 2007, *ApJS*, 171, 101
- Kartha, S. S., Forbes, D. A., Spitler, L. R., et al. 2014, *MNRAS*, 437, 273
- Kruijssen, J. M. D. 2009, *A&A*, 507, 1409
- Kruijssen, J. M. D. & Lamers, H. J. G. L. M. 2008, *A&A*, 490, 151
- Kundu, A. & Whitmore, B. C. 2001, *AJ*, 121, 2950
- Lada, C. J. & Lada, E. A. 2003, *ARA&A*, 41, 57
- Lamers, H. J. G. L. M., Baumgardt, H., & Gieles, M. 2010, *MNRAS*, 409, 305
- Lamers, H. J. G. L. M., Gieles, M., Bastian, N., et al. 2005, *A&A*, 441, 117
- Larsen, S. S., Brodie, J. P., Huchra, J. P., Forbes, D. A., & Grillmair, C. J. 2001, *AJ*, 121, 2974
- Majewski, S. R., Patterson, R. J., Dinescu, D. I., et al. 2000, in *Liege International Astrophysical Colloquia*, Vol. 35, *Liege International Astrophysical Colloquia*, ed. A. Noels, P. Magain, D. Caro, E. Jehin, G. Parmentier, & A. A. Thoul, 619
- Maraston, C. 2005, *MNRAS*, 362, 799
- Maxwell, A. J., Wadsley, J., Couchman, H. M. P., & Sills, A. 2014, *MNRAS*, 439, 2043
- Mieske, S. & Hilker, M. 2003, *A&A*, 410, 445
- Mieske, S., Hilker, M., & Infante, L. 2005, *A&A*, 438, 103
- Mieske, S., Jordán, A., Côté, P., et al. 2006, *ApJ*, 653, 193
- Mieske, S., Jordán, A., Côté, P., et al. 2010, *ApJ*, 710, 1672
- Milone, A. P., Marino, A. F., Cassisi, S., et al. 2012a, *ApJ*, 754, L34
- Milone, A. P., Marino, A. F., Piotto, G., et al. 2012b, *ApJ*, 745, 27
- Milone, A. P., Piotto, G., Bedin, L. R., et al. 2012c, *ApJ*, 744, 58
- Misgeld, I., Hilker, M., & Mieske, S. 2009, *A&A*, 496, 683
- Misgeld, I., Mieske, S., & Hilker, M. 2008, *A&A*, 486, 697
- Murray, N. 2009, *ApJ*, 691, 946
- Nomoto, K., Hashimoto, M., Tsujimoto, T., et al. 1997, *Nuclear Physics A*, 616, 79
- Park, H. S. 2012, *Journal of Korean Astronomical Society*, 45, 71
- Peng, E. W., Jordán, A., Côté, P., et al. 2006, *ApJ*, 639, 95
- Piotto, G., Milone, A. P., Anderson, J., et al. 2012, *ApJ*, 760, 39
- Piotto, G., Villanova, S., Bedin, L. R., et al. 2005, *ApJ*, 621, 777
- Raimondo, G., Brocato, E., Cantiello, M., & Capaccioli, M. 2005, *AJ*, 130, 2625
- Schiavon, R. P., Caldwell, N., Conroy, C., et al. 2013, *ApJ*, 776, L7
- Sippel, A. C., Hurley, J. R., Madrid, J. P., & Harris, W. E. 2012, *MNRAS*, 427, 167
- Spitler, L. R., Larsen, S. S., Strader, J., et al. 2006, *AJ*, 132, 1593
- Strader, J., Brodie, J. P., Spitler, L., & Beasley, M. A. 2006, *AJ*, 132, 2333
- Strader, J. & Smith, G. H. 2008, *AJ*, 136, 1828
- Usher, C., Forbes, D. A., Spitler, L. R., et al. 2013, *MNRAS*, 436, 1172
- Ventura, P., D’Antona, F., Mazzitelli, I., & Gratton, R. 2001, *ApJ*, 550, L65
- Wehner, E. M. H., Harris, W. E., Whitmore, B. C., Rothberg, B., & Woodley, K. A. 2008, *ApJ*, 681, 1233
- Willman, B. & Strader, J. 2012, *AJ*, 144, 76
- Woosley, S. E. & Weaver, T. A. 1995, *ApJS*, 101, 181